

A well-established harmony in chaos: from isolated galaxies to galaxy clusters

Caglar, T.

Citation

Caglar, T. (2022, December 21). A well-established harmony in chaos: from isolated galaxies to galaxy clusters. Retrieved from https://hdl.handle.net/1887/3503643

Version: Publisher's Version

Licence agreement concerning inclusion of doctoral thesis License:

in the Institutional Repository of the University of Leiden

Downloaded from: https://hdl.handle.net/1887/3503643

Note: To cite this publication please use the final published version (if applicable).

6 BASS XXXV. The $M_{\rm BH}$ - σ_{\star} Relation of Type 1 AGNs from 105-Month Swift-BAT survey

Adapted from Caglar, T. et al. in prep.

Abstract

We present two independent measurements of stellar velocity dispersions (σ_{\star}) from the Ca II H+K + Mg I region (3880–5550 Å) and the Calcium Triplet region (CaT, 8350–8750 Å) for 173 hard X-ray selected Type 1 AGNs from the second data release of the Swift/BAT AGN Spectroscopic Survey (BASS DR2). We construct one of the largest samples of local Type 1 AGNs using single-epoch (SE) black hole mass $(M_{\rm BH})$ and σ_{\star} measurements obtained from high-resolution data, which make it one of the best data sets currently available. The resulting $\sigma_{\rm CaT}$ estimates are found to be very consistent with the ones from the $\sigma_{\rm CaH+K+MgI}$ for our AGNs sample (an average offset of 0.002 ± 0.001 dex). We find that the extinction in the broad-line region (BLR) causes an under-estimation of $M_{\rm BH}$ (on average ~ 0.12 dex) in the SE-based measurements of our sample of Type 1 AGNs, consequently, an over-estimation of Eddington ratios (log $\lambda_{\rm Edd}$). We also find an anti-correlation between the offset from the $M_{\rm BH}$ - σ_{\star} relation and the Eddington ratio according to the Spearman rank-order correlation statistics (ρ = -0.51 and ρ -value< 0.01). We report that our sample of Type 1 AGNs shows a shallower $M_{\rm BH}$ - σ_{\star} relation (a power law exponent of \sim 3.50) relative to inactive galaxies, confirming earlier results obtained from smaller samples.

6.1 Introduction

Supermassive black holes (SMBHs), residing in the centers of massive galaxies, are commonly thought to co-evolve with their host galaxies as demonstrated by the present-day correlations between SMBH mass ($M_{\rm BH}$) and several host properties (e.g., McConnell & Ma 2013b; Kormendy & Ho 2013b), such as the stellar velocity dispersion (σ_{\star}) (Ferrarese & Merritt 2000b; Gebhardt et al. 2000; Merritt & Ferrarese 2001a; Tremaine et al. 2002; Gültekin et al. 2009; McConnell et al. 2011), bulge luminosity (Dressler 1980; Kormendy & Richstone 1995b; Marconi et al. 2004a), bulge mass (Magorrian et al. 1998; Häring & Rix 2004) and dark matter halos (Powell et al. 2022). Additionally, correlations with the bulge average spherical density and half-mass radius (e.g., Saglia et al. 2016), are also proposed in other works. Of these,

the $M_{\rm BH}$ - σ_{\star} relation is still the tightest relation among them (with an intrinsic scatter of ~ 0.3 dex; e.g., Kormendy & Ho 2013b).

The first observational evidence of the $M_{\rm BH}$ - σ_{\star} relation (Ferrarese & Merritt 2000b; Gebhardt et al. 2000) is attributed to be a result of AGN feedback by theoretical models, linking the growth of galaxy bulge and SMBH. These models predict a relation based on a parameter α ($M_{\rm BH} \propto \sigma_{\star}^{\alpha}$), which is suggested to be $\alpha \simeq 4$ for momentum driven feedback and $\alpha \simeq 5$ for energy-driven feedback (Silk & Rees 1998b; King 2003, respectively). However, the exact feedback mechanism responsible for achieving such a strong correlation remains highly debated. In one of the previous investigations, Kormendy & Ho (2013b, henceforth KH13) find a relation $M_{\rm BH} \propto \sigma_{\star}^{4.38}$ using spatially resolved gas and stellar kinematics for elliptical and classical bulge hosting local galaxies. However, McConnell & Ma (2013b, henceforth MM13) report an $M_{\rm BH} \propto \sigma_{\star}^{5.64}$ relation using $M_{\rm BH}$ estimates from spatially resolved dynamics based on their sample, that comprises early and late-type galaxies (including brightest cluster galaxies) in the local universe. Here, we note that both samples are dominated by inactive galaxies with the presence of just a few low-luminous AGNs. Finally, van den Bosch (2016b) report an $M_{\rm BH} \propto \sigma_{\star}^{5.35}$ relation using a sample of galaxies in which SMBH masses are compiled using four different methods: gas dynamics, stellar dynamics, reverberation mapping and megamasers.

On the other hand, there is an ongoing debate whether these relations depend on galaxy morphology, i.e., early-late McConnell & Ma (2013b), pseudo-elliptical bulge (Greene et al. 2010b; Kormendy & Ho 2013b; Ho & Kim 2014) and barred-unbarred (Graham 2008; Graham & Li 2009; Xiao et al. 2011; Beifiori et al. 2012b). Interestingly, some studies have shown an $M_{\rm BH} \propto \sigma_{\star}^{-3}$ relation for host galaxies with pseudo bulges (e.g., Greene et al. 2010b; Ho & Kim 2014). But, pseudo-bulge hosting galaxies are found to have an order of magnitude lower black hole masses relative to elliptical bulge hosting galaxies (e.g., Greene et al. 2010b; Ho & Kim 2014). They are found to reside below the $M_{\rm BH}$ - σ_{\star} relation of inactive galaxies and show a relatively higher scatter at the lower-mass end.

Additionally, reverberation mapping (RM) has been used for measuring $M_{\rm BH}$ for AGNs showing broad-emission lines (e.g., Blandford & McKee 1982b; Peterson 1993b; Onken & Peterson 2002b; Denney et al. 2006b, 2010b; Bentz et al. 2006b, 2009d,b, 2016b; Villafaña et al. 2022). However, even with the many dedicated observing campaigns in the last few decades, the number of black hole masses estimated using RM method is still limited to \approx 90 AGNs (see the RM black hole mass archive Bentz & Katz 2015). Here, we note that there are ongoing RM campaigns aiming to obtain RM-based black hole mass estimates for larger AGN samples, such as OzDES-RM (Yuan et al. 2015) and SDSS-RM (Shen et al. 2015, 2016).

The so-called single-epoch (SE) $M_{\rm BH}$ estimation method provides a potential solution to estimate black hole masses for the large spectroscopic samples of Type 1 AGNs. The method provides a simple (but successful) way of measuring black hole masses using the width of a broad emission line as a proxy of the BLR gas cloud velocities and the AGN continuum luminosity as a probe of the broad-line region (BLR) radius. The strong relationships between the radius of the BLR and the monochromatic AGN continuum luminosities at various wavelengths (i.e., 1350, 3000, 5100 Å) are shown in many studies (Koratkar & Gaskell 1991; Kaspi et al. 2000b, 2005; Bentz et al. 2006c, 2009d; Shen & Liu 2012b; Kozłowski 2017b; Zajaček et al. 2020). The uncertainty in the SE method is found to be $\gtrsim 0.40$ dex (Pancoast et al. 2014b; Ricci et al. 2017e; Caglar & Hudaverdi 2017a), which is mostly dominated by the intrinsic scatter in the $M_{\rm BH}$ - σ_{\star} relation.

By assuming that AGNs and inactive galaxies follow the same relation, an average multiplicative offset from the $M_{\rm BH}$ - σ_{\star} relation, which is defined as the f factor, is obtained for RM samples. An average $f_{\rm FWHM}$ factor of ≈ 1 is reported with an uncertainty of 0.15 dex for calibrating RM-based $M_{\rm BH}$ estimations (e.g., Onken et al. 2004b; Woo et al. 2013b, 2015b). Converting the virial product estimates from the RM method to actual $M_{\rm BH}$ estimates using the f factor, the $M_{\rm BH}$ - σ_{\star} is constructed for AGN hosting galaxies in numerous studies (Nelson et al. 2004b; Onken et al. 2004b; Woo et al. 2010b, 2013b, 2015b; Graham

et al. 2011b; Park et al. 2012b; Batiste et al. 2017c; Bennert et al. 2021). The slope of the $M_{\rm BH}$ - σ_{\star} relation is found to be shallower ($\sim \sigma_{\star}^{<4}$) for AGN samples relative to inactive galaxies (e.g., Woo et al. 2013b, 2015b), but the discrepancy between the two relations is assumed to be due to unreliable σ_{\star} estimates for the AGN sample, as well as due to sample selection bias (Greene & Ho 2006b; Lauer et al. 2007; Shen 2013; Shankar et al. 2016). Unfortunately, the assumption that the $M_{\rm BH}$ - σ_{\star} relations of active and inactive galaxies are the same, is a necessity to convert virial products from the RM sample to actual black hole masses. However, it is not widely accepted whether AGNs and inactive galaxies should follow the same scaling relation since the dynamically determined $M_{\rm BH}$ estimates suffer from the resolution-dependent bias for inactive galaxies, while AGNs do not suffer from the same bias (Bernardi et al. 2007; Shankar et al. 2016). The physical reasons behind the discrepancy between the $M_{\rm BH}$ - σ_{\star} relations of AGNs and inactive galaxies are not yet fully understood, and the comparisons with larger samples are further needed to address the origin of such discrepancies.

In this work, we provide stellar velocity dispersion estimations of Type 1 AGNs from the second data release of the Swift/BAT AGN Spectroscopic Survey (BASS DR2, Koss et al. 2022b). We aim to study the $M_{\rm BH}$ - σ_{\star} relation for our sample and compare our results with the $M_{\rm BH}$ - σ_{\star} relation for inactive galaxies. We additionally intend to discuss possible reasons for offset (if any exists) from the $M_{\rm BH}$ - σ_{\star} relation constructed from local inactive galaxies (log $M_{\rm BH,BLR}$ - log $M_{\rm BH,\sigma} = \Delta M_{\rm BH}$) using various AGN physical parameters. This paper is organized as follows. In Section 6.2, we introduce the BASS sample and archival data. In Section 6.3, we explain our analysis and methods. In Section 6.4, we present and discuss our results. Finally, in section 6.5, we present our main findings and conclusions. Throughout this paper, we assume a Λ CDM cosmology with the following parameters: $H_0 = 70 \, \mathrm{km \, s^{-1} \, Mpc^{-1}}$, $\Omega_{\rm M} = 0.3$ and $\Omega_{\Lambda} = 0.7$ for a flat universe.

6.2 BASS Sample and Archival Data

The Swift-BAT hard X-ray (14 – 195 keV) all-sky survey consists of \sim 858 AGNs for the 70-month data release (Baumgartner et al. 2010). As a part of BASS DR2, we aim to provide the optical spectra for each AGN in the 70-month catalog. The targeted spectroscopic observations via optical spectroscopy cover a wide spectral range (3000-10000 Å), in order to study both broad/narrow emission lines and host galaxy properties. In addition, the hard X-ray Swift-BAT survey allows us to detect AGNs with a wide range of neutral hydrogen absorbing columns: from unabsorbed (log $N_{\rm H} < 22~{\rm cm}^{-2}$) to Compton-thick (log $N_{\rm H} > 24~{\rm cm}^{-2}$) sources. More detailed information about the BASS DR2 can be found in the BASS catalog and overview papers (Koss et al. 2022b,a).

6.2.1 Our sample

The BASS DR2 sample comprises 858 AGNs; 359 type 1, 393 type 2 AGNs (including Seyfert 1.9 AGNs), and 106 beamed and/or lensed AGNs (see Koss et al. 2022b,a, for more details). For interested readers, we note that the velocity dispersion estimations for the BASS DR2 obscured AGNs (Type 1.9 and 2 AGNs) are presented in Koss et al. (2022c). In this work, we select only Type 1 AGNs with a redshift $z \leq 0.08$ due to contamination with telluric lines affecting the CaT spectral features beyond this redshift. This results in a selection of 263 Type 1 AGNs from the 70-month catalog.

For the 70-month catalog, there are only 6 missing observations (highly extincted AGNs located at the galactic latitude |b| < 10), whereas the spectroscopic observations are still ongoing for a significant portion of AGNs in the 105-month survey. We additionally exclude 71 Type 1 AGN spectra observed with low-resolution instruments (R < 1000) from our

sample. We note that we limit our completeness measurements to the 70-month study. Conclusively, our final sample consists of a total number of 241 AGNs, of which there are 186 Type 1 AGNs from the 70-month catalog and a bonus sample of 55 Type 1 AGNs from the 105-month survey. Here, we emphasize that the BASS sample is unbiased compared to other surveys with respect to obscuration (reaching Compton-thick levels: $N_{\rm H} \sim 10^{24} {\rm ~cm^{-2}}$, Koss et al. 2016; Ricci et al. 2017c) and star-formation (Ichikawa et al. 2017, 2019; Koss et al. 2021)

6.2.2 BASS archival data

6.2.2.1 X-ray, Infrared, and Radio Data

We adopt hydrogen column density ($N_{\rm H}$) and intrinsic (absorption-corrected) X-ray luminosity estimates for 70-month Swift-BAT sources reported from Ricci et al. (2017a). They are obtained by fitting the X-ray spectra with a combination of models including an absorbed cutoff power-law component, an unobscured reflection component, and another cutoff power-law component for scattering. Finally, Ricci et al. (2017a) provides the resulting $N_{\rm H}$ estimates within 90% confidence intervals and the intrinsic (absorption-corrected) X-ray luminosities.

For the AGNs in the 70-month Swift-BAT at high galactic latitudes ($|b| > 10^{\circ}$), the IR luminosities associated with emission driven by the AGN heated dust and by star-formation ($L_{\rm IR}^{\rm AGN}$ and $L_{\rm IR}^{\rm SF}$, respectively) are obtained individually for 587 non-beamed AGNs through IR spectral energy distribution decomposition by Ichikawa et al. (2017, 2019). We first adopt $L_{\rm IR}^{\rm SF}$ estimates from Ichikawa et al. (2017, 2019) for type 1 AGNs in our sample. We then convert $L_{\rm IR}^{\rm SF}$ estimates to the star-formation rates (SFRs) using the $L_{\rm IR}^{\rm SF}$ -SFR conversion by Kennicutt (1998). Our SFR sample consists of 99 AGNs from the Swift-BAT 70-month catalog. However, since we are also interested in the star formation at the central region, we additionally focus on Herschel/PACS detected sources, which leaves us 49 AGN from the Swift-BAT 70-month catalog.

Radio fluxes at 22 GHz for 28 type 1 AGNs in our sample were drawn from Smith et al. (2016, 2020), who observed 100 BAT AGNs with the Jansky Very Large Array in C configuration. The resultant spatial resolution of 1" corresponds to 0.5 kpc at z=0.025 (the median z for the 28 AGN in common with our sample), which is sufficient to resolve the core radio AGN luminosities and should be powered predominantly by the central engine.

6.2.2.2 Black Hole Mass Archive

We adopt SE black hole mass estimates of our sample of AGNs from Mejía-Restrepo et al. (2022), who fit the emission line profiles using the procedure explained in Trakhtenbrot & Netzer (2012) and Mejía-Restrepo et al. (2016). In Mejía-Restrepo et al. (2022), black hole masses are calculated using SE black hole mass calibrations provided by Greene & Ho (2005, for H α) and Trakhtenbrot & Netzer (2012, for H β) adopting an FWHM-based virial factor f=1. In the following, we present the adopted H α -based prescription for $M_{\rm BH}$ from Mejía-Restrepo et al. (2022).

$$M_{\rm BH} = 2.67 \times 10^6 \times \left(\frac{L[{\rm b}H\alpha]}{10^{42}~{\rm erg~s^{-1}}}\right)^{0.55 \pm 0.02} \times \left(\frac{FWHM[{\rm b}H\alpha]}{10^3~{\rm km\,s^{-1}}}\right)^{2.06 \pm 0.06}~M_{\odot} \tag{6.1}$$

A detailed explanation and a full list of fitting parameters can be found in Mejía-Restrepo et al. (2022).

6.3 Analysis and Methods

6.3.1 Stellar Velocity Dispersion Estimations

We apply the penalized pixel-fitting (pPXF) routine to obtain stellar velocity dispersions for our sample of Type 1 AGNs (Cappellari & Emsellem 2004b; Cappellari 2017b). The pPXF routine applies the Gauss-Hermite parametrization for the line-of-sight velocity distribution in the pixel space. By using pPXF, the continuum can be matched using additive polynomials, whereas bad pixels and/or emission lines can be masked from the spectra. Finally, pPXF makes initial guesses for stellar velocity dispersion by broadening stellar templates. During this procedure, the pPXF fitting parameters : V, σ , h_1 , ..., h_m , where V is velocity, σ is stellar velocity dispersion and h_i is the i-th Hermite polynomial, are fitted simultaneously.

In our study, we performed pPXF fitting routine using VLT/X-shooter spectral template (Chen et al. 2014b) adopting h_1 and h_2 Hermite polynomials. The X-shooter Spectral Library contains 830 stellar spectra of 683 stars covering the wavelength range 3500 - 24800 Å with an average instrumental resolution of 0.51 Å for the blue part of spectra (3800-5500 Å) and 0.78 Å for the red-side of spectra (8300-8800 Å). However, our sample of galaxies is observed by various instruments with a variety of spectral resolutions (Palomar/Double Spectrograph low-resolution: $\sim 4.0\,\text{ Å}$ (3800-5500 Å) - 6.0 Å (8300-8800 Å), Palomar/Double Spectrograph high-resolution: $\sim 2.3 \text{ Å} (3800\text{-}5500 \text{ Å}) - 2.0 \text{ Å} (8300\text{-}8800 \text{ Å}), \text{VLT/X-shooter: } \sim 2.1 \text{ Å}$ $(3800-5500 \text{ Å}) - 2.65 \text{ Å} (8300-8800 \text{ Å}), \text{SDSS}: \sim 2.5 \text{ Å} (3800-5500 \text{ Å}) - 2.7 \text{ Å} (8300-8800 \text{ Å}),$ $Keck/LRIS: \sim 4.0 \text{ Å} (8300-8800 \text{ Å}), SOAR/Goodman: \sim 2.0 \text{ Å} (8300-8800 \text{ Å}).$ Therefore, the template spectra are convolved with a relative line-spread function. We masked AGN emission lines (H ϵ 3970 Å, Ne[III] 3968 Å, H δ , H γ , H β , O[III] 4959 and 5007 Å, O I 8446 Å, Fe II 8616 Å) and bad-pixels (if any exists) to increase the accuracy of stellar velocity dispersion estimations. In order to mask broad emission components, we additionally apply a mask function with a range of width: $2000-3500 \text{ km s}^{-1}$ considering the BLR width of the selected broad-line AGN. Finally, pPXF fittings are repeated 100 times by randomly sampling the residuals of the best fit of pPXF for obtaining the uncertainty in stellar velocity dispersion estimations.

We present the results of stellar velocity dispersion measurements from the region covering Ca H+K and Mg I, and/or the CaT (henceforth σ_{Red} and σ_{Blue} , respectively) for our sample of AGNs. Additionally, the resulting pPXF fitting images are presented in appendix 6.G. These fittings are visually inspected by three co-authors: TC, LB, and MK. Finally, we provide a quality flag (0 for good quality fits, 1 for acceptable fits, and 2 for unaccepted fits) for each AGN spectrum. For the majority of sources, we were able to fit both the blue part and the red part of the spectra for obtaining σ_{\star} estimates. For the SOAR data, we only fit the CaT region to obtain the stellar velocity dispersion since the instrumental setup only covers the CaT region.

6.3.2 Extinction in the BLR

In SE $M_{\rm BH}$ estimators, either monochromatic or line luminosity (e.g., L_{5100} or $L_{\rm H}\alpha$) is used as a probe of BLR radius, which allows us to estimate $M_{\rm BH}$. These prescriptions are fundamentally based on RM studies, in which the targets are assumed to be unobscured, Type 1 AGNs. However, in case of the presence of dust extinction, a correction should be applied to the observed line luminosities. In previous work, Caglar & Hudaverdi (2017a, henceforth C20) demonstrated that such an extinction-related correction reduces the average offset from the $M_{\rm BH}-\sigma_{\star}$ relation ~ 0.3 dex from $M_{\rm BH}-\sigma_{\star}$ relation for their sample of AGNs.

In Section 6.4.2.1, we discuss the importance of extinction correction in the BLR-based $M_{\rm BH}$ estimations. We use intrinsic hard X-ray luminosities for obtaining extinction-corrected H α luminosities assuming that the extinction of H α emission is purely due to attenuation by

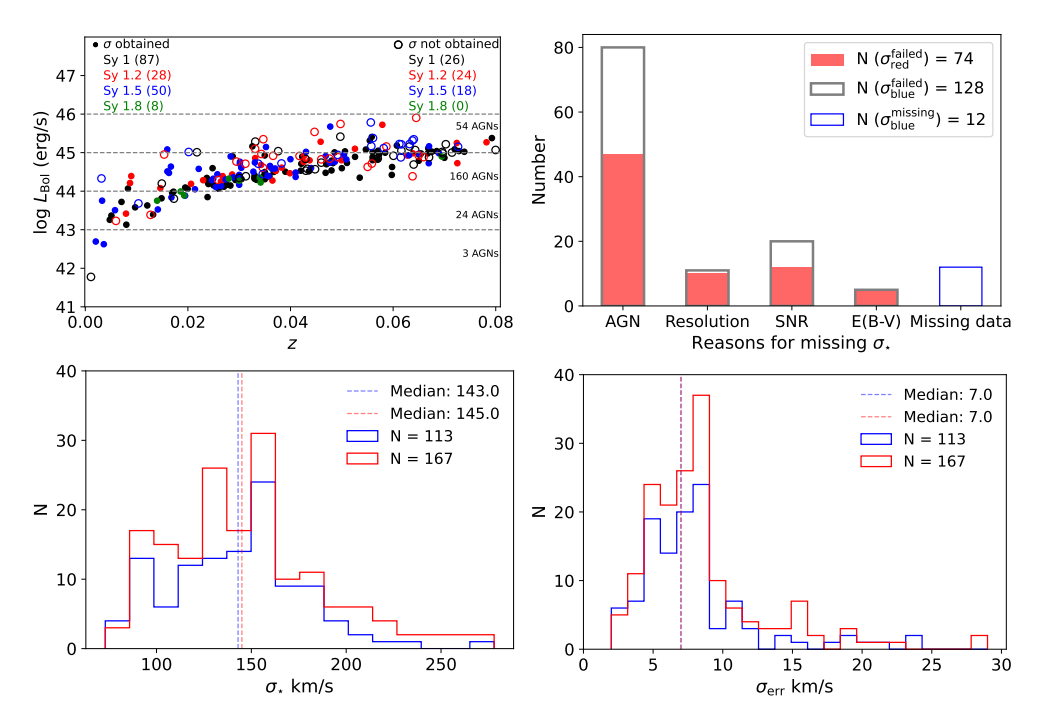


Figure 6.1: The bolometric AGN luminosities versus redshift for our sample of AGNs. We show AGNs with successful σ_{\star} fits with a filled circle, whereas the ones with failed σ_{\star} fits are shown with open circles (top left). Distributions of failed σ_{Blue} (focusing on the region covering the Ca H+K and Mg I absorption lines) and σ_{Red} (focusing on the region covering the Calcium triplet absorption lines) measurements are separated by the reason causing the failure (top right). Distributions of successful velocity dispersion fit results (bottom left) and measurement errors (bottom right) for our sample of AGNs. The blue histograms represent the $\sigma_{\rm Blue}$, whereas the red histograms represent the $\sigma_{\rm Red}$.

dust (Shimizu et al. 2018):

$$\log L_{\text{Ho}[\text{corr}]} = 1.17 \log L_{\text{X}, 14-150 \text{ keV}} - 6.61,$$
 (6.2)

where $\log L_{\rm X, \, 14-150 \, keV}$ is the intrinsic X-ray luminosity at 14 - 150 keV energy band and $\log L_{\rm H\alpha[corr]}$ is the intrinsic H α luminosity. Here, we note that we adopt the updated $\log L_{\rm X, \, 14-150 \, keV}$ - $\log L_{\rm H}$ correlation parameters (T. Shimizu, private communication), and this method introduces an additional ~ 0.1 dex systematical uncertainty in $M_{\rm BH}$ measurements. We then use the observed and corrected H α luminosities for estimating the BLR extinction as:

$$A_{\text{H}\alpha} = 2.5(\log L_{\text{H}\alpha,\text{corr}} - \log L_{\text{H}\alpha,\text{obs}}). \tag{6.3}$$

We use the empirically determined extinction law (Wild et al. 2011) to derive extinction in any wavelength λ following:

$$\frac{A_{\lambda}}{A_{\rm V}} = 0.6 \left(\frac{\lambda}{5500}\right)^{-1.3} + 0.4 \left(\frac{\lambda}{5500}\right)^{-0.7}.$$
 (6.4)

We note that this equation provides a good correction for AGNs with a large dust reservoir (Wild et al. 2011; Schnorr-Müller et al. 2016; Caglar & Hudaverdi 2017a).

6.3.3 Eddington Ratio and Accretion Rates

In order to estimate Eddington ratios (log $\lambda_{\rm Edd}$), we follow the same approach used in BASS DR1 Koss et al. (2017b). First, we convert the intrinsic, absorption-corrected hard X-ray luminosities ($L_{\rm X,\,2-10\,keV}$) to $L_{\rm Bol}$ using the following equation: $L_{\rm Bol}=L_{\rm X,\,2-10\,keV}\times c$, where c is a typical bolometric correction factor ($c\approx20^{+60}_{-10}$) for luminous AGNs (Marconi et al. 2004b; Vasudevan et al. 2009). Here, we note that the adopted bolometric correction factor is fairly constant for low luminosity AGNs (log $L_{\rm X,\,2-10\,keV}<45$ erg s⁻¹) in Swift-BAT catalog (Duras et al. 2020), since the majority of our sample is domained by such low-luminosity AGNs. We then estimate the Eddington Luminosity ($L_{\rm Edd}$) using the following formula: $L_{\rm Edd}=1.26\times10^{38}\,M_{\rm BH}/M_{\odot}$. Finally, we divide $L_{\rm Bol}$ by $L_{\rm Edd}$ to obtain log $\lambda_{\rm Edd}$. Here, we emphasize that the large uncertainty in $L_{\rm Bol}$ (~0.30 -0.60 dex) and $M_{\rm BH}$ (~0.40 dex) contribute to the uncertainty of Eddington ratio, which is likely $\gtrapprox0.7$ dex in total. We also estimate the physical accretion rates (\dot{M}) that power the AGN in our sample, through $\dot{M}=L_{\rm Bol}/\left(\epsilon c^2\right)$, assuming a radiative efficiency of $\epsilon=0.1$.

6.4 Results and Discussion

In this work, we provide stellar velocity dispersion estimates of the BASS DR2 Type 1 AGNs sample. In the top left panel of Figure 6.1, we give an overview of our sample of AGNs for successful (173) and failed (68) σ_{\star} fit results. The majority of stellar velocity dispersion estimates are obtained from the CaT (167 successful and 74 failed fits), but whenever available, we provide the resulting stellar velocity dispersion estimates from the blue part of the spectra focusing on the Ca H+K and Mg I absorption lines (113 successful and 116 failed fits. There are also 12 missing fits since five of them do not cover the target wavelength range due to our observational setup and seven of the σ_{\star} estimates are adopted from the LLAMA study by C20). Additionally, we discuss the issues related to sample (in)completeness; present a comparison between the σ_{Blue} and σ_{Red} measurements, explore the systematic uncertainties caused by aperture size, and show a direct comparison of σ_{\star} with other surveys. Using the BASS archival data, we discuss the possible reasons for the offset from the $M_{\rm BH}$ - σ_{\star} relation for physical parameters, such as the BLR extinction, redshift, the intrinsic X-ray luminosity, SFR, the core radio AGN luminosity at 22 GHz, and Eddington ratio. Finally, we present the resulting $M_{\rm BH}$ - σ_{\star} relation for our sample of Type 1 AGNs.

6.4.1 Stellar Velocity Dispersion Estimations

6.4.1.1 Sample (in-)completeness

Thanks to the high-resolution observations with instruments such as VLT/X-shooter, Soar/Goodman, and Palomar/Double Spectrograph, our sample is bias-free from issues caused by instrumental resolution insufficiency. The instruments used for this work provide an instrumental resolution of $\sigma_{\rm inst}$ =19 - 27 km s⁻¹. Some of our AGNs have been observed with lower spectral resolution as mentioned in Section 6.3.1. As can be seen from the top right panel of Figure 6.1, the σ_{\star} fitting failed for only a few Type 1 AGNs (\sim 11% for 241 AGNs) due to low instrument resolution.

Using the pPXF routine, we fit a total number of 241 Type 1 AGN spectra for two distinct optical regions (3880-5500 Å and 8350-8730 Å, whenever possible). We obtained at least one σ_{\star} estimate for 173 AGNs (see the top left panel of Figure 6.1) with 68 failed attempts (see Figure 6.1). For the 173 successful fits, we flag 128 stellar velocity dispersion estimates as good, 35 as acceptable, and 10 as bad fits. We additionally fit 48 duplicate spectra observed with other instruments (28 successful and 20 failed fits). We present the resulting σ_{\star} estimates from both optical regions with a quality flag. The main reasons for

failed σ_{\star} measurements are strong AGN features (\sim 69%), the limited signal-to-noise ratio (SNR) (\sim 15%), resolution insufficiency (\sim 11%), and the high galactic extinction (\sim 5%) (see the top right panel of Figure 6.1).

The resulting σ_{Red} estimates are found to be in the range: $73 \le \sigma_{Red} \le 278 \text{ km s}^{-1}$ with a median of $145\pm7 \text{ km s}^{-1}$, whereas the σ_{Blue} estimates are found to be in the range: $82 \le \sigma_{Blue} \le 272 \text{ km s}^{-1}$ with a median of $143\pm7 \text{ km s}^{-1}$, for our AGN sample. In the bottom panel of Figure 6.1, we present the distributions of stellar velocity dispersion estimates and their corresponding errors. We then compared the stellar velocity dispersion estimates from the CaT region and the independent estimates from the Ca H+K + Mg I absorption lines. They are found to be strongly correlated ($\rho = 0.98$, p-value< 0.01) according to Spearman statistics and very consistent with each other. The average offset between two σ_{\star} measurements is found to be 0.002±0.001 dex. The intrinsic scatter (from the 1:1 relation) is found to be $\epsilon = 0.027$ dex and such scatter is probably due to the different stellar populations in between these regions (e.g., Riffel et al. 2015b). In the left panel of Figure 6.2, we present the comparison between these.

6.4.1.2 Comparison With Other Measurements

We compare our best σ_{\star} estimates to the literature measurements from the Hyperleda stellar velocity dispersion catalog, which contains a total number of 39217 stellar velocity dispersion measurements for 29063 objects. We find a total number of 39 stellar velocity measurements from the Hyperleda stellar velocity dispersion catalog, which is a compilation of the following studies Nelson & Whittle (1995); Terlevich et al. (1990); Oliva et al. (1995, 1999); Wegner et al. (2003); Garcia-Rissmann et al. (2005); Greene & Ho (2006b); Ho et al. (2009); Cappellari et al. (2013). In the right panel of Figure 6.2, we present a comparison between our best σ_{\star} estimates and measurements from Hyperleda. As it can be seen from the right panel of Figure 6.2, our σ_{\star} measurement errors are relatively smaller than the ones from Hyperleda. Numerically, for overlapping sources, the median σ_{\star} value is $139\pm6~{\rm km\,s}^{-1}$ for our measurements, whereas the median is found to be $135\pm12~{\rm km\,s}^{-1}$ for the Hyperleda measurements. Finally, the difference between our σ_{\star} estimates and the ones from Hyperleda is found to be 0.02 dex. The difference in σ between our and Hyperleda measurements is probably caused by aperture differences.

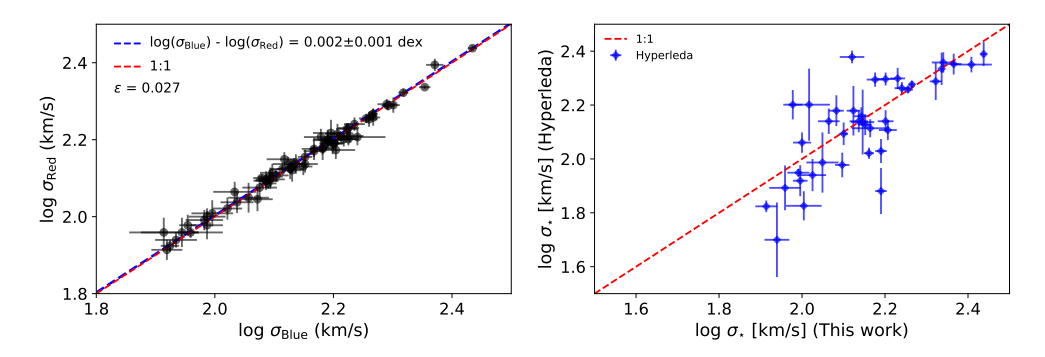


Figure 6.2: The comparison between σ_{Blue} and σ_{Red} (left), the comparison between our best fitting σ_{\star} results versus the σ_{\star} results in the literature (right).

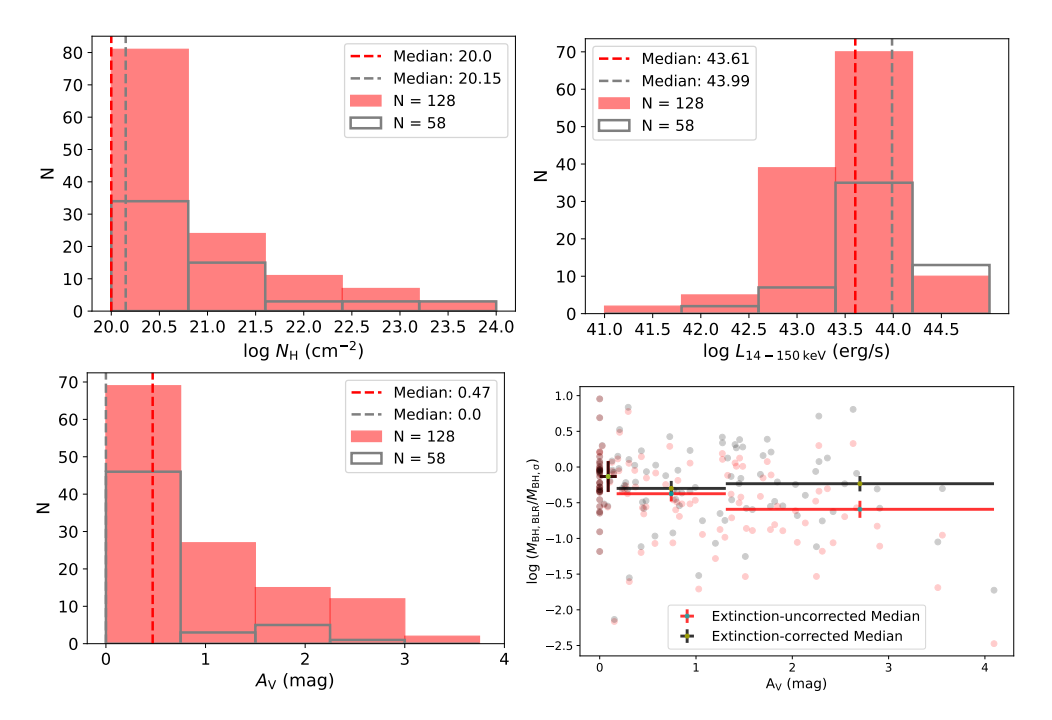


Figure 6.3: The distribution of hydrogen column density (top left), hard X-ray luminosity (top right) and the extinction in the BLR (bottom left). The red columns represent the presented parameter's distribution for AGNs with the successful σ_{\star} fits, whereas the grey ones represent the ones with failed σ_{\star} fits. Median values are presented as red and grey dashed vertical lines, respectively. Bottom right: the offset from the $M_{\rm BH}$ - σ_{\star} relation versus the extinction in the BLR for our sample of AGNs. The medians (and errors) are presented for three bins with equal numbers of data points

6.4.2 The offset from the $M_{\rm BH}$ - σ_{\star} relation

6.4.2.1 The Extinction in the BLR

Assuming that the extinction in broad $L_{\rm H\alpha}$ is entirely linked to dust obscuration and further assuming that the Galactic $N_{\rm H}/A_{\rm V}$ ratio is 1.79-2.69 \times 10^{21} cm⁻² (Predehl & Schmitt 1995; Nowak et al. 2012), we expect a maximum $N_{\rm H}$ threshold of $\sim 10^{22.3}$ cm⁻² for Type 1 AGNs (excluding Sy 1.9s) for discriminating X-ray absorbed and unabsorbed sources as described in Burtscher et al. (2016b). Here, we note that there are only 10 absorbed AGNs in our sample (see the top left panel of Figure 6.3). The median and mean $N_{\rm H}$ for our sample of AGNs are found to be 20.0 and 20.73 cm⁻², respectively. Here, we note that the majority of our $N_{\rm H}$ estimates clusters around log $N_{\rm H}=20.0$ cm⁻² because this is the limit (not a measurement) due to galactic extinction.

we mention that We also stress that we have no Compton-thick source $(N_{\rm H}>24~{\rm cm}^{-2})$ in our sample.

This allows us to use the observed X-ray luminosities as a probe of the extinction-corrected theoretical H α luminosities. In the top right panel of Figure 6.3, we present the distribution of hard X-ray luminosities in the 14 - 150 keV energy band ($L_{\rm X,\,14-150\,keV}$) in which the median and mean $L_{\rm X,\,14-150\,keV}$ are found to be 43.63 and 43.57 erg s⁻¹, respectively. The difference between the theoretical and observed H α luminosities, accordingly, gives us the X-ray-derived extinction in the BLR. The resulting median and mean $A_{\rm V}$ values are found to be 0.44 and 0.84 mag, respectively (see the bottom left panel of Figure 6.3). Our result shows that a good fraction (56%) of our AGNs has lower $A_{\rm V}$ than 1 mag. We also stress that there are only 16 AGN with $A_{\rm V}$ higher than 2 mag. Here, we stress that extinction correction has a very large uncertainty for such sources. Therefore, we suggest that extinction correction should be used with caution for such sources.

In the bottom right panel of Figure 6.3, we present the offset from the $M_{\rm BH}$ - σ_{\star} relation reported by KH13 ($\Delta M_{\rm BH} = \log M_{\rm BH,BLR}/M_{\rm BH,\sigma}$) versus the BLR extinction estimates for both extinction-uncorrected and extinction-corrected data sets. We find a negative trend (also shown by the Spearman correlation parameters: $\rho = -0.35$, p-value< 0.01) showing that the extinction in the BLR plays a role in the offset. Applying extinction-correction reduces the $\Delta M_{\rm BH}$ to some extent, but the $\Delta M_{\rm BH}$ still exists for each data bin (see Figure 6.3). This result is a confirmation of the C20's findings, in which the authors used a smaller sample selected from the 105-month Swift-BAT AGNs with a redshift cutoff z< 0.01 and a hard X-ray luminosity cutoff $\log L_{\rm X,~14-195~keV} \geq 42.5~{\rm erg~s^{-1}}$. Here, we emphasize that applying the extinction-correction increases the uncertainty of $M_{\rm BH}$ measurements in any case, but also, the variability between X-ray and optical emission from the BLR can cause an over-correction by up to $\sim 1~{\rm dex}$ for some sources.

For the individual case of NGC 1365 (BAT 184, $\log L_{\rm H\alpha} = 39.37~{\rm erg~s^{-1}}$ and $A_{\rm H\alpha} = 3.40~{\rm mag}$), the extinction-corrected $\log L_{\rm H\alpha}$ is estimated as 40.73 erg s⁻¹, which means an increase of $\log L_{\rm H\alpha}$ of 1.36 dex. Correspondingly, the extinction-corrected $M_{\rm BH}$ differs from the extinction-uncorrected $M_{\rm BH}$ by 0.75 dex for NGC 1365. This result confirms that the extinction in the BLR can cause under-estimation of $M_{\rm BH}$ for highly obscured AGNs unless it is taken into account. This result is also shown by C20 and recent DR2 BASS papers Ricci et al. (2022); Mejía-Restrepo et al. (2022). Here, we note that NGC 1365 is a well-known changing look AGN (e.g., Risaliti et al. 2000, 2009; Mondal et al. 2022; Temple et al. 2022).

6.4.2.2 Redshift and the intrinsic X-ray Luminosity

In Figure 6.4, we present a direct comparison between z and $L_{\rm X, 14-150 \, keV}$ versus $\Delta M_{\rm BH}$ for both extinction-uncorrected and extinction-corrected data. We see the increasing trends between z and $L_{\rm X, 14-150 \, keV}$ versus $\Delta M_{\rm BH}$ for both extinction-uncorrected and extinction-corrected data. For redshift versus $\Delta M_{\rm BH}$, Spearman correlation coefficients (ρ) are found to

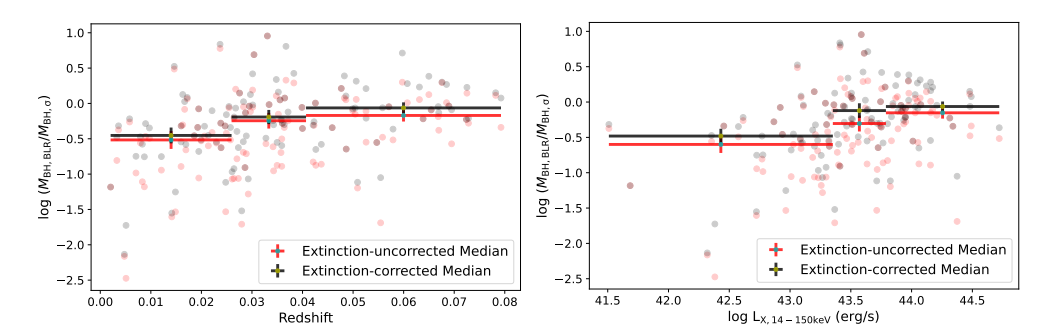


Figure 6.4: Left: The comparison between the $\Delta M_{\rm BH}$ and redshift. Right: The comparison between the offset from the $M_{\rm BH}$ - σ_{\star} relation and hard X-ray luminosity. The medians (and errors) are presented for three bins with equal numbers of data points.

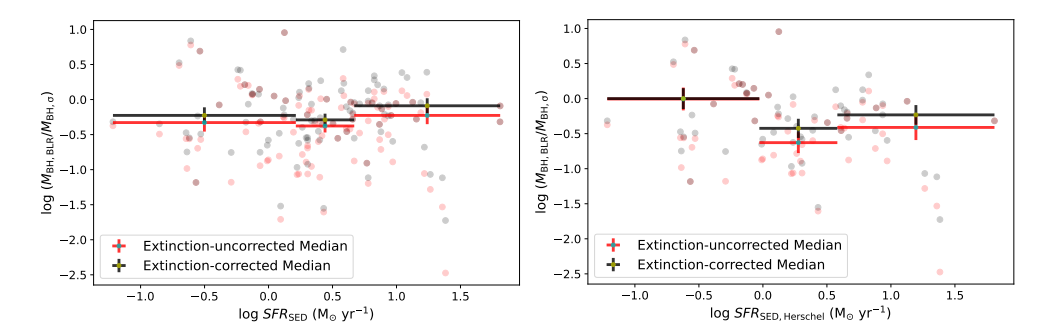


Figure 6.5: Left: The comparison between the $\Delta M_{\rm BH}$ and SFRs. Right: Same with only Herschel/PACS data. The medians (and errors) are presented for three bins with equal numbers of data points.

be 0.38 and 0.44 for the extinction-uncorrected and extinction-corrected data, respectively. Additionally, the resulting Spearman correlation coefficients for $L_{\rm X, \, 14-150 \, keV}$ versus $\Delta M_{\rm BH}$ are found to be 0.32 and 0.41 for the extinction-uncorrected and extinction-corrected data, respectively. The resulting p-values are found to be smaller than 0.01 for all cases implying that the observed correlation is unlikely to be due to chance. However, the trend here is very likely due to a selection bias due to the flux-limited nature of the BAT survey. As z increases, the chance of detecting lower luminosity sources decreases. In fact, we can observe in Table 6.3 that redshift ($\log(1+z)$) is strongly correlated with $L_{\rm Bol}$ ($\rm r_s\sim 0.82$) which indicates a strong redshift-luminosity selection bias. We also stress that some contribution to this trend might come from projection effects caused by the limitation of instrumental aperture sizes since the $M_{\rm BH}$ - σ_{\star} relation is assumed to hold at effective radii. The $M_{\rm BH}$ estimates from the BLR are not affected by such limitations, since BLR gas resides at sub-parsec scales.

6.4.2.3 Outflows and Star-formation

Energy-driven outflows can have a strong influence on host galaxy evolution. Such outflows can easily sweep huge amounts of gas away from the galaxy and shut down star formation. Therefore, galaxies can rapidly transform from star-forming to quiescent galaxies (see the review by Morganti 2017, and the references therein). On the other hand, outflows can also increase star formation via rapid cooling of swept material and/or the compression of disks (Zubovas et al. 2013; Zubovas & King 2019). Remarkably, AGN and star formation

are connected to each other, however, the physical cause of this connection is still unclear. In the nearby universe, the majority of AGN-hosting galaxies are low-mass galaxies with moderate SFRs (Schawinski et al. 2007; Zubovas & King 2019). In such systems, black holes are growing via secular processes and minor mergers, and the amount of energy produced by the AGN may not be sufficient to affect their host galaxies. However, major dry mergers can cause rapid growth in black hole mass, correspondingly, this process can decrease $\Delta M_{\rm BH}$ (see the review by KH13). Here, we emphasize that such major mergers are rare in the nearby universe (e.g., Governato et al. 1999; Conselice 2014).

As discussed in previous studies, galaxies hosting pseudo-bulges show a significant offset from the $M_{\rm BH}$ - σ_{\star} relation of elliptical/classical bulge hosting galaxies (Greene et al. 2010b; Beifiori et al. 2012b; Kormendy et al. 2011b; Kormendy & Ho 2013b). AGNs are found to be in the transition region between the blue and red cloud, referred as green valley (Schawinski et al. 2007; Lacerda et al. 2020). KH13 suggests that star formation is expected in AGNs, and the presence of young stars can increase the offset from the $M_{\rm BH}$ - σ_{\star} relation. In recent work, Burtscher et al. (2021) have shown that the major contribution to starlight comes from the old stellar populations (in the majority of cases, the young stellar fraction is less than 5%) using the local luminous AGNs and matched analogs (see Davies et al. 2015b, for LLAMA sample). Similar trends are also seen in other recent works (Mallmann et al. 2018; Riffel et al. 2021, 2022, and the references therein).

Here, we test whether star formation in AGN systems causes an offset from the $M_{\rm BH}$ - σ_{\star} relation. In Figure 6.5, we present the comparison between SFR and $\Delta M_{\rm BH}$. Using the estimated SFRs from infrared SED fitting (Ichikawa et al. 2017, 2019) for all and Herschel data sets, we do not find any significant relation between the $\Delta M_{\rm BH}$ and SFRs for our sample of AGNs. For all data, the median SFR bins show a flat profile for both extinction-uncorrected and extinction-corrected data with the resulting Spearman correlation coefficients: $\rho = -0.03$ (p-value> 0.10) and $\rho = 0.01$ (p-value> 0.10), respectively. We additionally limit our sample to the Herschel data, which consists of 49 AGNs from the 70-month catalog. As can be seen in the right panel of Figure 6.5, we also report flat trends between SFR and $\Delta M_{\rm BH}$ for both extinction-uncorrected and extinction-corrected data. This is also confirmed by the resulting Spearman correlation coefficients: $\rho = -0.24$ (p-value> 0.10) for extinction-uncorrected and $\rho = -0.18$ (p-value> 0.10) for extinction-corrected data. Here, we stress that our SFR measurements are obtained at different distance scales from sub-kpc to several kpc, SFR in the nuclear scale can still be responsible for the $\Delta M_{\rm BH}$.

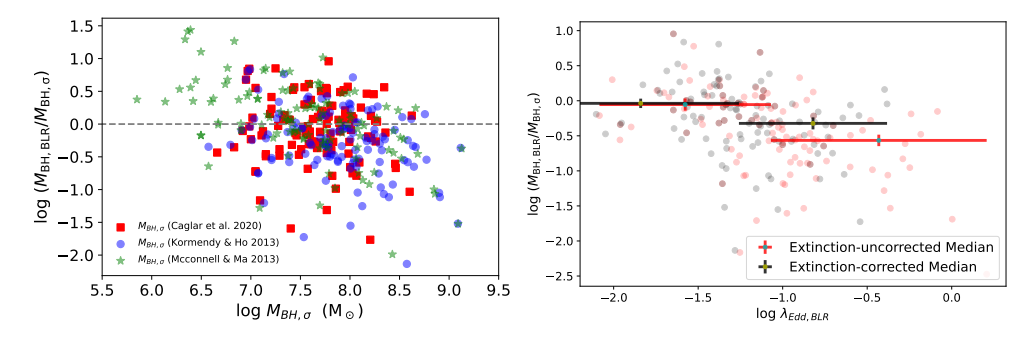


Figure 6.6: The comparison between the adopted the $M_{\rm BH}$ - σ_{\star} relation as an estimator of $M_{\rm BH}$ (left). The $\Delta M_{\rm BH}$ versus Eddington ratio (right). The medians (and errors) are presented for two bins in which we exactly match them in terms of the number of data points.

6.4.2.4 The $M_{\rm BH}$ estimators

A considerable problem with the $M_{\rm BH}$ - σ_{\star} relation is the slope of the relation. The slope is very important, because it can be attributed to the exact feedback mechanism responsible for achieving such a relation (e.g., $M_{\rm BH} \propto \sigma^4$ for momentum-driven AGN feedback and $M_{\rm BH} \propto \sigma^5$ for energy-driven AGN feedback, King 2003; Silk & Rees 1998b). In previous efforts for achieving a universal $M_{\rm BH}$ - σ_{\star} relation, a wide range of slopes is reported in various studies; $\beta = 4.80 \pm 0.50$ (Ferrarese & Merritt 2000b), $\beta = 3.75 \pm 0.30$ (Gebhardt et al. 2000), $\beta = 4.02 \pm 0.32$ (Tremaine et al. 2002), $\beta = 4.24 \pm 0.41$ (Gültekin et al. 2009), $\beta = 4.42 \pm 0.3$ (Beifiori et al. 2012b), $\beta = 3.46 \pm 0.61$ (AGNs, Woo et al. 2013b), $\beta = 3.97 \pm 0.56$ (AGNs, Woo et al. 2015b), $\beta = 4.38 \pm 0.29$ (Kormendy & Ho 2013b), $\beta = 5.64 \pm 0.32$ (McConnell & Ma 2013b), $\beta = 3.90 \pm 0.93$ (Batiste et al. 2017c) and $\beta = 3.38 \pm 0.65$ (AGNs, Caglar & Hudaverdi 2017a).

Apparently, adopting different scaling relations result in an additional ~ 0.35 dex difference (for a hypothetical $\sigma_{\star}=150~{\rm km\,s^{-1}}$) in $M_{\rm BH}$ estimations, even though the intrinsic scatter of the $M_{\rm BH}$ - σ_{\star} relation is really tight ($\epsilon \sim 0.3~{\rm dex}$) in many of these studies. This effect can be somewhat larger (> 0.80 dex) for the lower and higher end of $M_{\rm BH}$ - σ_{\star} relation. In the left panel of Figure 6.6, we compare our $M_{\rm BH}$ estimates obtained from three different scaling relations (C20, KH13, and MM13) versus the $\Delta M_{\rm BH}$. Here, it is worth mentioning that the KH13 sample is compiled using elliptical/classical bulge hosting galaxies, whereas the MM13 sample consists of early and late-type galaxies, as well as BCGs. On the other hand, the C20 sample consists of the hard X-ray selected most luminous local Type 1 AGNs (LLAMA). It appears that black hole masses obtained using the $M_{\rm BH}$ - σ relation reported by C20 are relatively closer to the zero point compared to the ones reported by KH13 and MM13. Using our sample of AGNs, we report that the scaling relation by KH13 shows a tendency to overestimate black hole masses, whereas the scaling relation by MM13 tends to underestimate black hole masses. This result indicates that AGNs might be following a different $M_{\rm BH}$ - σ_{\star} relation.

6.4.2.5 The Eddington Ratio and Accretion Rates

In this section, we investigate whether the $\Delta M_{\rm BH}$ is correlated with the Eddington ratio. First, we report the estimated extinction-uncorrected Eddington ratios in a logarithmic range of -2.1< $\log \lambda_{\rm Edd} < 0.21$. The logarithmic median Eddington ratio is found to be $\log \lambda_{\rm Edd} \sim$ -1.01, whereas we only have two sources higher than $\log \lambda_{\rm Edd} > 0$ (NGC 1365 and PKS0521-36). There are high extinction ($A_{\rm V} > 3.5$ mag) for both of these sources, therefore, $M_{\rm BH}$ values are under-estimated due to the BLR extinction (accordingly, $\log \lambda_{\rm Edd}$ values are overestimated). Excluding high $A_{\rm V}$ sources ($A_{\rm V} > 1$ mag), we only have four AGNs exceeding $\log \lambda_{\rm Edd} > -0.5$ (Mrk359, 2MASXJ08551746-2854218, Mrk783, 2MASXJ21344509-2725557). We then correct our $\log \lambda_{\rm Edd}$ estimates for the BLR extinction. The resulting extinction-corrected Eddington ratio ($\log \lambda_{\rm Edd,corr}$) estimates are found to be in a logarithmic range of -2.43 < $\log \lambda_{\rm Edd,corr} < -0.37$ with a median $\log \lambda_{\rm Edd,corr}$ of -1.16. This result is very consistent with other works proposing that high Eddington ratio AGNs are rare in the nearby universe (Heckman et al. 2004; Ho 2009).

In the right panel of Figure 6.6, we present the comparison between the $\Delta M_{\rm BH}$ versus the Eddington ratio. We show the extinction-corrected and extinction uncorrected $M_{\rm BH}$ and $\log \lambda_{\rm Edd}$ estimates. We divide data points into two bins with equal numbers of data points. The median $\log \lambda_{\rm Edd}$ values show a decreasing trend for both extinction corrected and uncorrected estimates. First, applying the BLR extinction correction actually increases $M_{\rm BH}$ estimates, accordingly, decreases the measured $\log \lambda_{\rm Edd} \sim 0.1$ dex on average. But for highly extincted AGNs ($A_{\rm V} > 2$ mag), the $\log \lambda_{\rm Edd}$ can be over-estimated ~ 0.4 dex which is even more dramatic for the highest obscured source in our survey; NGC 1365($A_{\rm V} = 4.1$ mag) resulting in an increase of $\log \lambda_{\rm Edd}$ by 0.75 dex. Finally, the Spearman rank-order correlation

-								
Feature	EV 1	EV 2	EV 3	EV 4	EV 5	EV 6	EV 7	
Variance	55.3%	25.0%	10.6%	3.9%	2.7%	2.2%	0.3%	
$\log \sigma_{\star}$	-0.33	-0.49	0.63	0.42	-0.7	-0.06	0.68	
$\log(1+z).$	-0.14	-0.46	0.37	0.11	-0.85	-0.30	0.83	
$\log L_{5100}$	0.17	-0.51	0.77	0.32	-0.47	-0.47	0.42	
$\log L_{\mathrm{H}\alpha}$	0.55	-0.79	0.47	-0.53	-0.12	-0.48	0.09	
$A_{ m V}$	-0.69	-0.01	0.15	0.56	-0.83	0.19	0.84	
$\log L_{ m Bol}$	-0.05	-0.68	0.54	< 0.01	-0.71	-0.26	0.68	
$\Delta M_{ m BH}$.	0.06	-0.27	-0.40	-0.83	0.43	0.39	-0.39	

Table 6.1: The resulting Spearman correlation coefficients between the select features for each Eigenvector (EV) from Principal Component Analysis.

statistics also confirm this trend with a resulting $\rho = -0.37$ (p-value < 0.01).

We now discuss the possibility that AGNs in the nearby universe are growing towards the $M_{\rm BH}$ - σ_{\star} relation. To understand this, we first measure the accretion rates of our AGNs. We report the resulting accretion rates in a range of $0.0007 < \dot{M} < 0.93 \rm\ M_{\odot}\ y^{-1}$ with a median of $0.058 \text{ M}_{\odot} \text{ y}^{-1}$. Our results are clearly showing that the majority of SMBHs of BAT Type 1 AGNs are growing with low accretion rates and at sub-Eddington levels. Here, if we assume that the offset from $M_{\rm BH}$ - σ_{\star} relation comes from the proposition that SMBHs still need to grow to keep up with their host galaxies, we can actually estimate the required AGN phase for achieving such relation. In this study, the median $M_{\rm BH}$ is found to be $\sim 10^{7.5}~M_{\odot}$ and the average $\Delta M_{\rm BH}$ is found to be 0.3 dex. This means a black hole growth time (AGN phase) of $\sim 10^{8.75}$ yr is needed for obtaining zero offset between the estimates from $M_{\rm BH,BLR}$ and $M_{\rm BH,M-\sigma_*}$. Considering the typical AGN lifetime of 10^{7-9} yr estimated from the Soltan argument (Soltan 1982; Martini & Weinberg 2001; Marconi et al. 2004b), and considering the recently proposed AGN lifetime ($\sim 10^5$ yr) estimated from the lag between the central engine becoming visible on X-rays and the required photo-ionization time of host-galaxy (Schawinski et al. 2015), achieving the zero offset by a secular growth with such small accretion rates is very unlikely. However, we note that AGNs are expected to show a wide range of accretion rates from sub-Eddington to super-Eddington levels during the AGN life cycle rather than a constant accretion rate (e.g., Soltan 1982).

6.4.3 Correlation Matrix and Principal Component Analysis

To determine which features are correlated, we compute the correlation matrix for the following physical parameters: σ_{\star} , $\log(1+z)$, $FWHM_{\rm H\beta}$, $L_{\rm H\beta}$, $M_{\rm BH,H\beta}$, $FWHM_{\rm H\alpha}$, $L_{\rm H\alpha}$, $M_{\rm BH,H\alpha}$, $N_{\rm H}$, $A_{\rm V}$, $L_{\rm Edd}$, $L_{\rm Bol}$, $\log\lambda_{\rm Edd}$, $\Delta M_{\rm BH}$. In Table 6.3, which can be found in the appendix, we present the correlation matrix computed using the Spearman rank-order correlation statistic. We provide three different color codes which show the significance of the correlation. The black and blue represent significant correlations with p-value smaller than 0.01 and 0.05, whereas the red represents the insignificant correlation with p-value larger than 0.10. For example, $FWHM_{\rm H\alpha}$ and $M_{\rm BH,H\alpha}$ or $L_{\rm H\beta}$ and $L_{\rm H\alpha}$ show strong correlations ($\rho=0.80$ and 0.91, respectively) with significant p-value< 0.01. These results are expected since the parameters in both comparisons are highly connected to each other by definition.

Interestingly, the BLR extinction $(A_{\rm V})$ shows a statistically significant (p-value < 0.01) correlation between $L_{\rm H\beta}$, L_{5100} , $L_{\rm H\alpha}$, $\log \lambda_{\rm Edd}$ with a resulting ρ of 0.51, 0.46, 0.56 and 0.40, respectively. However, the $A_{\rm V}$ shows an anti-correlation between $\Delta M_{\rm BH}$ with a resulting ρ = -0.35 (p-value < 0.01). For z, we also see a statistically significant (p-value < 0.01) strong correlation between $L_{\rm H\beta}$, L_{5100} , $L_{\rm H\alpha}$, $L_{\rm Edd}$, $L_{\rm Bol}$ and $\Delta M_{\rm BH}$ $(\rho = 0.59, 0.62, 0.69, 0.60, 0.82$ and 0.42 respectively). This result implies that as z increases, so does the luminosity. This is

probably a selection bias caused by flux-limited surveys. Based on the correlation coefficients, the $\log \lambda_{\rm Edd}$ and $A_{\rm V}$, show an anti-correlation with $\Delta M_{\rm BH}$.

In order to identify the main parameters that are driving the variance in our data set, we conduct a Principal Component Analysis (PCA) for the following parameters: σ_{\star} , $\log(1+z)$, $FWHM_{\rm H\alpha}$, L_{5100} , $L_{\rm H\alpha}$, $A_{\rm V}$, $L_{\rm Bol}$ and $\Delta M_{\rm BH}$. Using four features, we can explain 94.8% variance in the data set. The most dominant one is the first eigenvector, which explains 55.3% variance. Other eigenvectors explain, 25.0%, 10.6%, 3.9%, 2.7%, 2.2% and 0.3% variance, respectively. By inspecting the correlations of these eigenvectors with the selected variables (see table 6.1,) we find that the first eigenvector is driven by anti-correlation between $A_{\rm V}$ and $L_{\rm H\alpha}$ indicating an obscuration effect in the observed $L_{\rm H\alpha}$ in agreement with previous works (Caglar & Hudaverdi 2017a; Ricci et al. 2022; Mejía-Restrepo et al. 2022). The anti-correlations between z, $L_{\rm H\alpha}$ and σ_{\star} mostly drive the second eigenvector. This indicates a selection bias from the flux-limited sample that favors the detection of high luminous and high σ_{\star} objects as z increases. The other eigenvectors only explain the 19.7% variance of the data set, and there are at least 5 dominant parameters for each eigenvector. This indicates that there is a significant scatter in the measured properties suggesting that they are driven by different parameters than the first and second eigenvector.

6.4.4 The $M_{\rm BH}$ - σ_{\star} relation of BAT Type 1 AGNs

We fit our data set using the bi-variate correlated errors and intrinsic scatter method, which takes into account the measurement errors in both X and Y axes (Akritas & Bershady 1996b; Nemmen et al. 2012). The linear regression was performed using the Y/X method, in which we allow to vary both the slope and intercept. We repeated the linear regression fits for 4 different sub-samples as follows: all AGNs without extinction correction, $A_{\rm V}=0$ mag, $A_{\rm V}<1$ mag, and all AGNs with extinction correction. In Table 6.2, we present the resulting intercept (α) , slope (β) , and intrinsic scatter ϵ of each sub-sample.

We perform the linear regression adopting the extinction-uncorrected $M_{\rm BH}$ and the best (good and acceptable fits mentioned in 6.3.1) σ_{\star} estimates from our entire data set (henceforth DS1), which has 158 data points. We also fit two sub-samples of unobscured sources from our sample: $A_{\rm V}=0$ and $A_{\rm V}<1$ mag, (henceforth DS2 and DS3, respectively), in which there are 31 and 72 data points. Finally, we repeated the linear regression adopting extinction-corrected $M_{\rm BH}$ and the best σ_{\star} estimates for obtaining the $M_{\rm BH}$ - σ_{\star} relation of 115 AGNs (henceforth DS4).

We find the slope of DS1 (2.94 \pm 0.41) smaller than the slope of other data sets (DS2: 3.50 \pm 0.79, DS3: 3.60 \pm 0.50 and DS4: 3.32 \pm 0.42). In Figure 6.11, we present the resulting $M_{\rm BH}$ - σ_{\star} relation for each data sets in the appendix. This result additionally shows that the extinction in the BLR plays an important role in the $\Delta M_{\rm BH}$.

Here, we emphasize that this is one of the largest $M_{\rm BH}$ - σ_{\star} investigations for type 1 AGNs. The resulting slope range is then found to be: $2.53 \le \beta \le 4.10$. The resulting slopes are very consistent with Caglar & Hudaverdi (2017a) in which authors report a slope of 3.38 ± 0.65 , an intercept of 8.14 ± 0.20 and an intrinsic scatter of 0.32 ± 0.06 for the LLAMA sample. Our slope is also consistent with the slope reported by Woo et al. (2013b, 3.46 ± 0.61 obtained from the RM sample). However, DS1 and DS4 are roughly consistent with the slope of 4.38 ± 0.29 reported by KH13. Also, the slopes obtained from all of our data sets are not consistent with the slope of 5.64 ± 0.32 reported by MM13. We additionally compare our result with one of the latest $M_{\rm BH}$ - σ_{\star} relations reported by Bennert et al. (2021) in which authors report a slope of 3.89 ± 0.53 using 29 RM AGNs and a slope of 4.55 ± 0.29 for 51 inactive galaxies. A direct comparison between our work and Bennert et al. (2021) shows consistency with the reported AGN $M_{\rm BH}$ - σ_{\star} slope within the uncertainty, but not consistent with the reported slope of inactive galaxies. This result indicates that AGNs show a shallower $M_{\rm BH}$ - σ_{\star} relation compared to inactive galaxies.

118 6.5. CONCLUSION

					_
Sub-sample ^{a}	Number	α	β	ϵ	-
All (no corr)	158	7.87 ± 0.08	2.94 ± 0.41	0.24 ± 0.05	_
$A_{\rm V} = 0$	31	8.19 ± 0.09	3.50 ± 0.79	$0.36{\pm}0.06$	a
$A_{\rm V} < 1$	72	8.13 ± 0.08	3.60 ± 0.50	$0.25{\pm}0.04$	
$A_{\rm V}$ (corrected)	115	8.10 ± 0.07	3.32 ± 0.42	$0.39 {\pm} 0.06$	_

Table 6.2: The list of columns for the final table of AGNs with duplicate σ_{\star} fits

6.5 Conclusion

In the flux-limited 105-month Swift-BAT catalog, we study Type 1 AGNs at $z \le 0.08$. Whenever available, we provide new measurements of stellar velocity dispersions, obtained for both the CaT and CaH+K + MgI region, for a total number of 173 AGNs. This work is one of the largest stellar velocity dispersion investigations for hard X-ray-selected Type 1 AGNs. Using the $M_{\rm BH}$ archive provided by Mejía-Restrepo et al. (2022), we compare our results with the established $M_{\rm BH}$ - σ_{\star} relations. We itemize our main results below:

- The average offset between σ_{Blue} and σ_{Red} measurements is found to be 0.002 ± 0.001 dex, which shows a great consistency between the σ_{\star} measurements from two distinct optical regions.
- We show that the BLR extinction plays a somewhat important role in a favor of the underestimation of black hole masses, and accordingly the over-estimations of Eddington ratios.
- We did not find any significant trend between the $\Delta M_{\rm BH}$ and SFR.
- After applying the extinction-correction to $M_{\rm BH}$ measurements, we find Eddington ratios in a range of -2.43< $\log \lambda_{\rm Edd} <$ -0.37. Additionally, we provide the resulting accretion rates in a range of $0.0007 \le \dot{M} \le 0.93~{\rm M}_{\odot}~{\rm y}^{-1}$ with a median of $0.058~{\rm M}_{\odot}~{\rm y}^{-1}$. This result shows that hard X-ray-selected BAT Type 1 AGNs are growing at Sub-Eddington levels.
- We provide an $M_{\rm BH}$ σ_{\star} relation for four different data sets. The resulting slopes are found to be significantly smaller than the slopes obtained from inactive galaxies. According to this result, we report that the hard X-ray selected Type 1 AGN sample shows a shallower $M_{\rm BH}$ σ_{\star} relation relative to the inactive galaxy sample. Correspondingly, we conclude that using the $M_{\rm BH}$ σ_{\star} relation determined from AGN samples would be a more proper approach for obtaining black hole masses for large AGN samples.

Acknowledgments

TC would like to thank Violetta Gamez Rosas for the very productive discussions.

Appendix

6.A Galaxy Morphologies and Aperture Correction

Derived central parameters are known to be dependent on the aperture selection of observations (reported by various works Jorgensen et al. 1995; Mehlert et al. 2003; Cappellari

^aNGC 7213 is removed from the data sets as suggested by C20.

et al. 2006; Falcón-Barroso et al. 2017b), since galaxies have radial gradients in the stellar velocity dispersion and radial velocity. Therefore, we investigate the importance of aperture correction using the following formula:

$$\frac{\sigma_{\rm ap}}{\sigma_{\rm e}} = \left(\frac{r_{\rm ap}}{r_{\rm e}}\right)^{\alpha} \tag{6.5}$$

where α is the slope, $r_{\rm e}$ is the effective radius, $r_{\rm ap}$ is the aperture radius adopted in our spectroscopic observations, $\sigma_{\rm ap}$ is the stellar velocity dispersion obtained at $r_{\rm ap}$ and $\sigma_{\rm e}$ is the stellar velocity dispersion at $r_{\rm e}$. Here, we note that the slope of this equation is reported to depend on the galaxy morphologies (and stellar masses for spiral galaxies, Falcón-Barroso et al. 2017b). We collect the morphologies for our sample galaxies from the literature (de Vaucouleurs et al. 1995; Vitores et al. 1996; Paturel et al. 2003; Deo et al. 2006; Nair & Abraham 2010; de Lapparent et al. 2011b; Lintott et al. 2011) and divide them into two categories: E-like and S-like. Considering the reported average stellar masses of BAT AGNs ($\log M_{\star} = 10.28 \pm 0.4 \ M_{\odot}$) by Koss et al. (2011), we subsequently adopt the reported α of -0.055 for elliptical-like (E+L) galaxies and 0.077 for spiral galaxies, respectively (Falcón-Barroso et al. 2017b). Finally, we collected K-band effective radii from the Two Micron All Sky Survey (Skrutskie et al. 2006b) to compute the correction factor mentioned above. We present the collected galaxy morphologies and the effective radii for our sample of galaxies.

In Figure 6.7, we demonstrate a direct comparison between the σ_{\star} estimates obtained from our instruments' aperture sizes and effective radii. We find an offset of -0.020±0.003 dex between $\sigma_{\rm e}$ and $\sigma_{\rm ap}$ for elliptical-like galaxies, whereas the offset is found to be 0.042±0.005 dex for spiral galaxies. As mentioned in Section 6.4.1.1, our median σ_{\star} error (\sim 0.021 dex) is statistically similar to the offset caused by aperture selection. Therefore, we stress that this is unlikely to lead to a large systematic error in σ_{\star} measurements, but it should be added to the total σ_{\star} error budget.

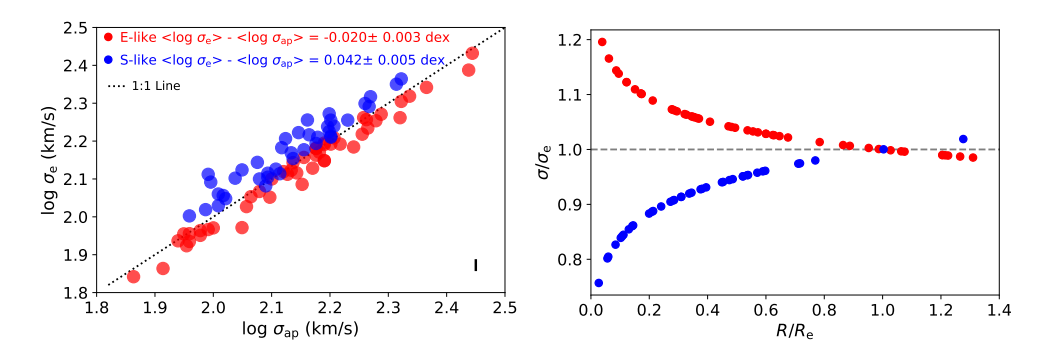


Figure 6.7: Left: The comparison between the σ_{\star} estimates obtained from our instruments' aperture sizes and effective radii. Right: The normalized stellar velocity dispersion profiles integrated within elliptical apertures with increasing semi-major radius.

6.B Comparison of the resulting σ_{\star} measurements from different instruments in our survey

In the bottom panel of Figure 6.8, we present a comparison of σ_{\star} measurements between various instruments used in our study. We find that our σ_{\star} measurements from different instruments are consistent with each other, for both $\sigma_{\rm Blue}$ and $\sigma_{\rm Red}$ measurements.

There is only one significant outlier from the 1:1 line in between the $\sigma_{\rm Blue}$ estimates, whereas there are two significant outliers for $\sigma_{\rm Red}$ estimates. The first outlier is BAT 197 (HE0351+0240) which shows ~ 0.10 dex difference in $\sigma_{\rm Red}$ measurements, whereas $\sigma_{\rm Blue}$ estimates remain significantly consistent with each other (a difference of ~ 0.01 dex). The second outlier is BAT 562 (NGC3822) which shows an offset of 0.09 dex in $\sigma_{\rm Blue}$ and 0.11 dex in $\sigma_{\rm Red}$ measurements, respectively. Here, we emphasize that such significant differences between σ_{\star} estimates can be caused by systematic uncertainties in some cases. These systematic uncertainties are likely caused by a combination of several factors, such as observational conditions, instrumental resolutions, spectral templates, spectral regions, and galaxy aperture sizes. We stress that the systematic uncertainties can be as large as the statistical uncertainties obtained from pPXF resampling and a detailed explanation of the systematic uncertainties is given by Koss et al. (2022c).

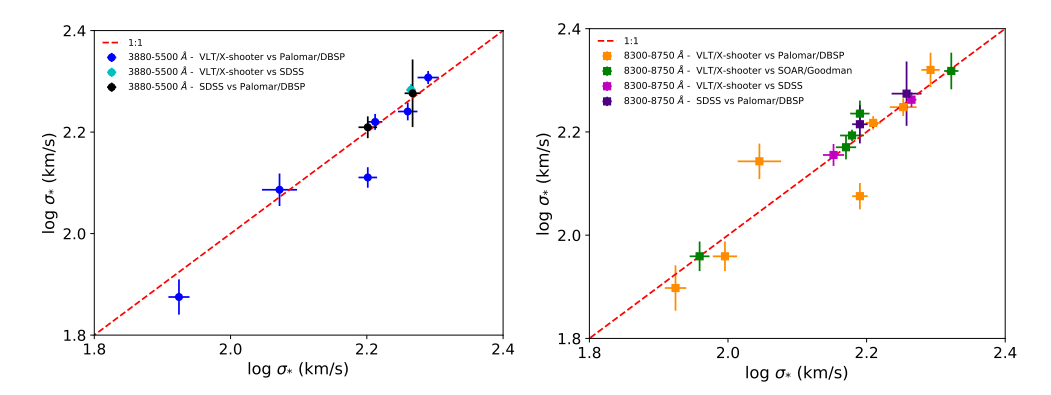


Figure 6.8: The comparison of σ_{\star} estimates between the instruments used in this study for 3880-5500 Å region (left) and 8350-8750 Å region (right). The red dashed lines represent the 1:1 lines for visual aid.

6.C The observed versus corrected black hole masses

In the left panel Figure 6.9, we present a comparison between the extinction in ${\rm H}\alpha$ (${\rm A}_{{\rm H}\alpha}$) versus the difference in black hole masses ($\log M_{{\rm BH,H}\alpha}^{corr}/M_{{\rm BH,H}\alpha}^{obs}$) after the extinction correction for our sample of AGNs. We show that the extinction in the BLR becomes somewhat important after ${\rm A}_{{\rm H}\alpha}\gtrsim 1$ mag. Luckily, the majority of our sample (81 out of 125) is found to have ${\rm A}_{{\rm H}\alpha}<1$ mag. In the right panel of Figure 6.9, we show the distribution of $\log M_{{\rm BH,H}\alpha}^{corr}/M_{{\rm BH,H}\alpha}^{obs}$ in which the median is found to be 0.107 dex. In only 27 cases, the difference is found to be 0.3 dex. Finally, we only have 6 AGNs showing $\log M_{{\rm BH,H}\alpha}^{corr}/M_{{\rm BH,H}\alpha}^{obs}$ > 0.5 dex.

6.D The core AGN Radio Luminosity versus the $\Delta M_{\rm BH}$

In previous efforts, radio-loud AGNs are found to show a high offset from the $M_{\rm BH}$ - σ_{\star} relation (e.g., Nelson 2000; Sheinis & López-Sánchez 2017). Using Type 1 AGNs from Smith et al. (2020) sample, we compare the radio luminosity and the $\Delta M_{\rm BH}$. Our sub-sample consists of 26 Type 1 AGNs in total, which is relatively large compared to previous studies with the same aim (e.g., Nelson 2000; Sheinis & López-Sánchez 2017). In previous studies, the $\sigma_{\rm OIII,\lambda5007}$ line has been used as a surrogate of σ_{\star} in order to increase the sample size (Shields

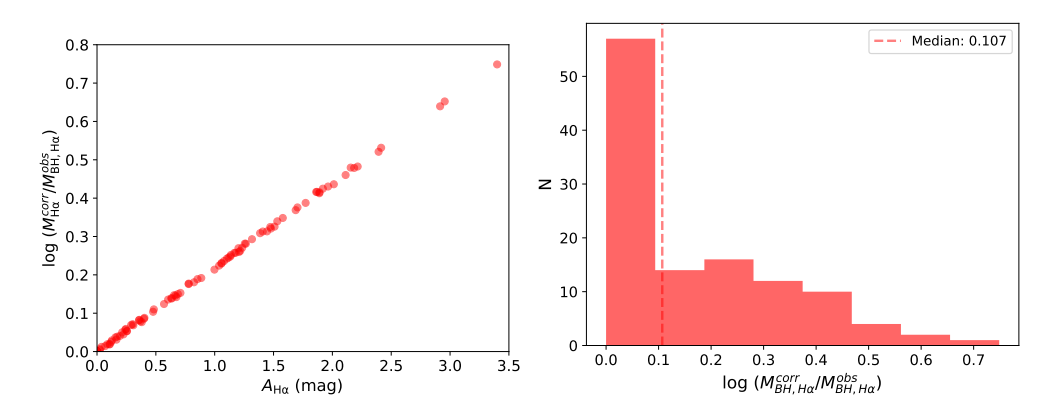


Figure 6.9: Left: the extinction in $H\alpha$ ($A_{H\alpha}$) versus the difference in black hole masses (log $M_{BH,H\alpha}^{corr}/M_{BH,H\alpha}^{obs}$) after the extinction-correction for our sample of AGNs. **Right:** the distribution of black hole mass differences after the extinction-correction.

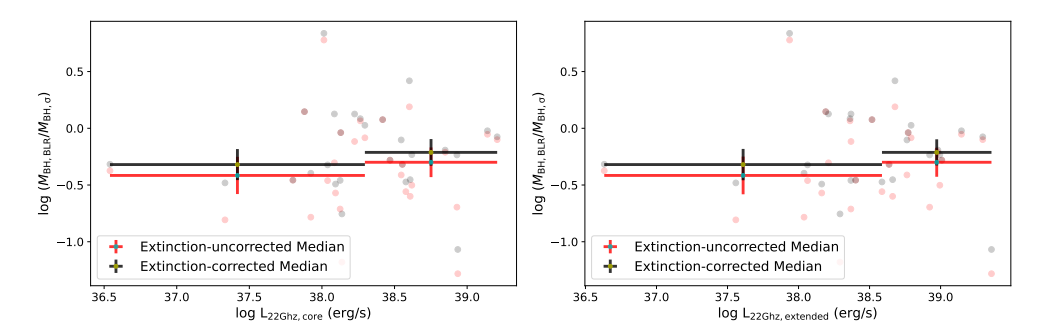


Figure 6.10: Left: The comparison between the $\Delta M_{\rm BH}$ and the core (1") radio AGN luminosity at 22 Ghz. Right: The $\Delta M_{\rm BH}$ versus the extended (6") radio AGN luminosity at 22 Ghz. The medians (and errors) are presented for three bins with equal numbers of data points.

et al. 2003; Boroson 2003; Bonning et al. 2005; Gu et al. 2009; Wu 2009; Gaur et al. 2019). However, this is controversial, since the [OIII] $\lambda 5007$ line profiles often show a non-Gaussian shape with a substantial asymmetry (e.g., Nelson & Whittle 1995).

In Figure 6.10, we present a comparison between $\Delta M_{\rm BH}$ versus the core AGN (1") luminosities from the 22 GHz band and the extended (6") radio AGN luminosity at 22 GHz. For both core and extended data, we present the comparisons with two median radio luminosity bins showing no significant trend for both extinction-uncorrected and extinction-corrected data sets. None of them are also significant based on the Spearman rank-order correlation statistics: $\rho < 0.09$ (p-value> 0.1). We emphasize that the high $M_{\rm BH}$ - σ_{\star} offset, which is found in radio-loud galaxies in previously mentioned studies, is probably caused by the high scatter in σ_{OIII} and σ_{\star} . But, we note that the sample is still not large enough to conclude any kind of correlation, and we leave this discussion for future studies.

6.E The resulting $M_{\rm BH}$ - σ_{\star} relation for all data sets

In Figure 6.11, we present the resulting $M_{\rm BH}$ - σ_{\star} relation fittings for all data sets: DS1 (extinction-uncorrected), DS2 ($A_{\rm V}=0$ mag), DS3 ($A_{\rm V}<1$ mag), DS4 (extinction-corrected). The resulting fits are shown within the 4σ confidence band.

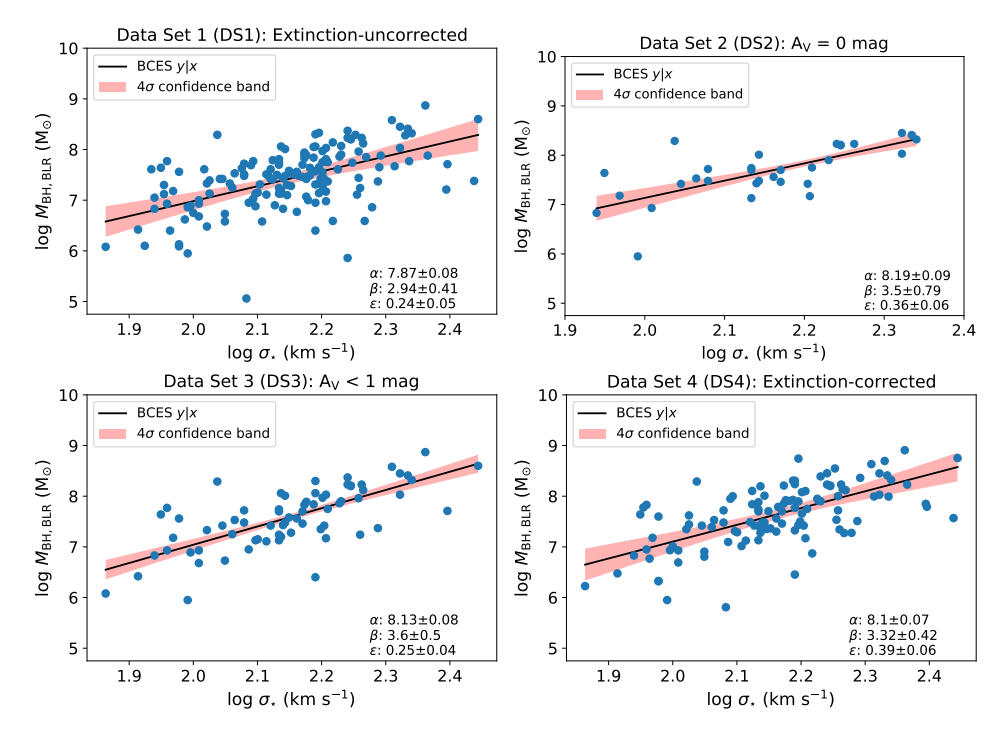


Figure 6.11: The $M_{\rm BH}$ - σ_{\star} relation of for different sub-samples in our sample: DS1 (top left), DS2 (top right), DS3 (bottom right), and DS4 (bottom right).

6.F The other histograms for successful and failed σ_{\star} attempts

In Figure 6.12, we present the distributions of z (top panel), L_{5100} (upper middle panel), $L_{\rm X, \, 14-195 \, keV}$ (lower middle panel) and Seyfert type (bottom panel) for successful and failed fits. In the top panel of Figure 6.12, we find that as z increases, the chance of obtaining a successful σ_{\star} fittings decreases for both the blue and red regions. Also, as luminosity (for both L_{5100} and $L_{\rm X, \, 14-195 \, keV}$) increases, the chance of obtaining a successful σ_{\star} fits decreases for both blue and red region (see the upper and lower middle panels of Figure 6.12). This result is probably due to two reasons: the presence of a strong AGN continuum and/or broad emission lines. Finally, we see no significant trend between the failed σ_{\star} estimates and Seyfert types (see the bottom panel of Figure 6.12).

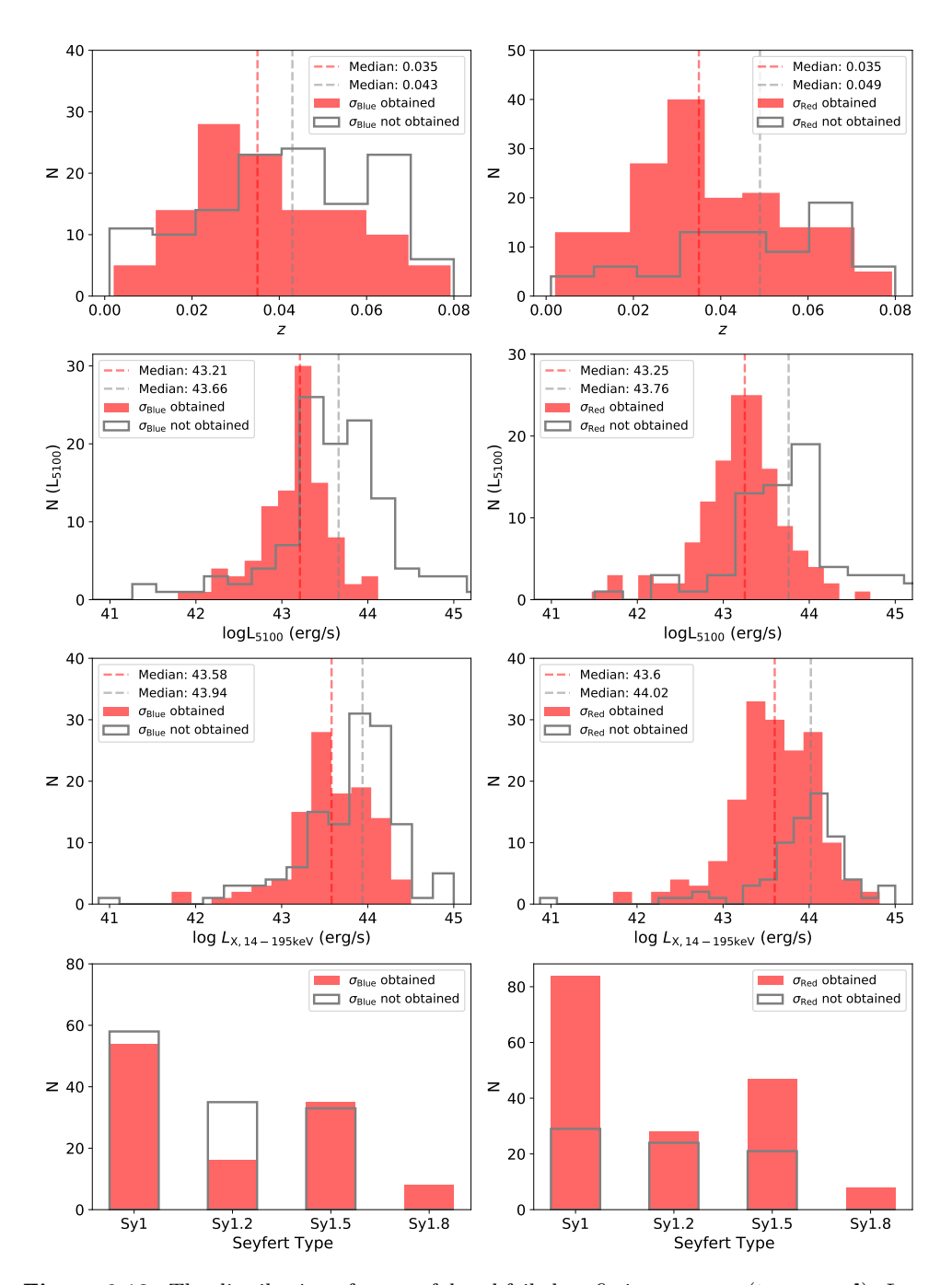


Figure 6.12: The distribution of successful and failed σ_{\star} fitting versus z (top panel), L_{5100} (upper middle panel), $L_{\rm X,\,14-195\,keV}$ (lower middle panel) and Seyfert type (bottom panel). The σ_{Blue} distributions are shown on the left panels, whereas the σ_{Red} distributions are presented on the right panels.

6.G Examples of pPXF fits

In Figure 6.13, we present three successful σ_{Blue} (left panel) and σ_{Red} (right panel) fitting plots. We also show an example of failed σ_{\star} fitting plots in Figure 6.14 for both σ_{Blue} and σ_{Red} . We note that these plots represent the most common setups.

6.H The Spearman rank-order correlation results.

In Table 6.3, we present the Spearman rank-order correlation results for all physical parameters used in this study. The table is presented with color codes of p-values for visual aid.

BIBLIOGRAPHY 125

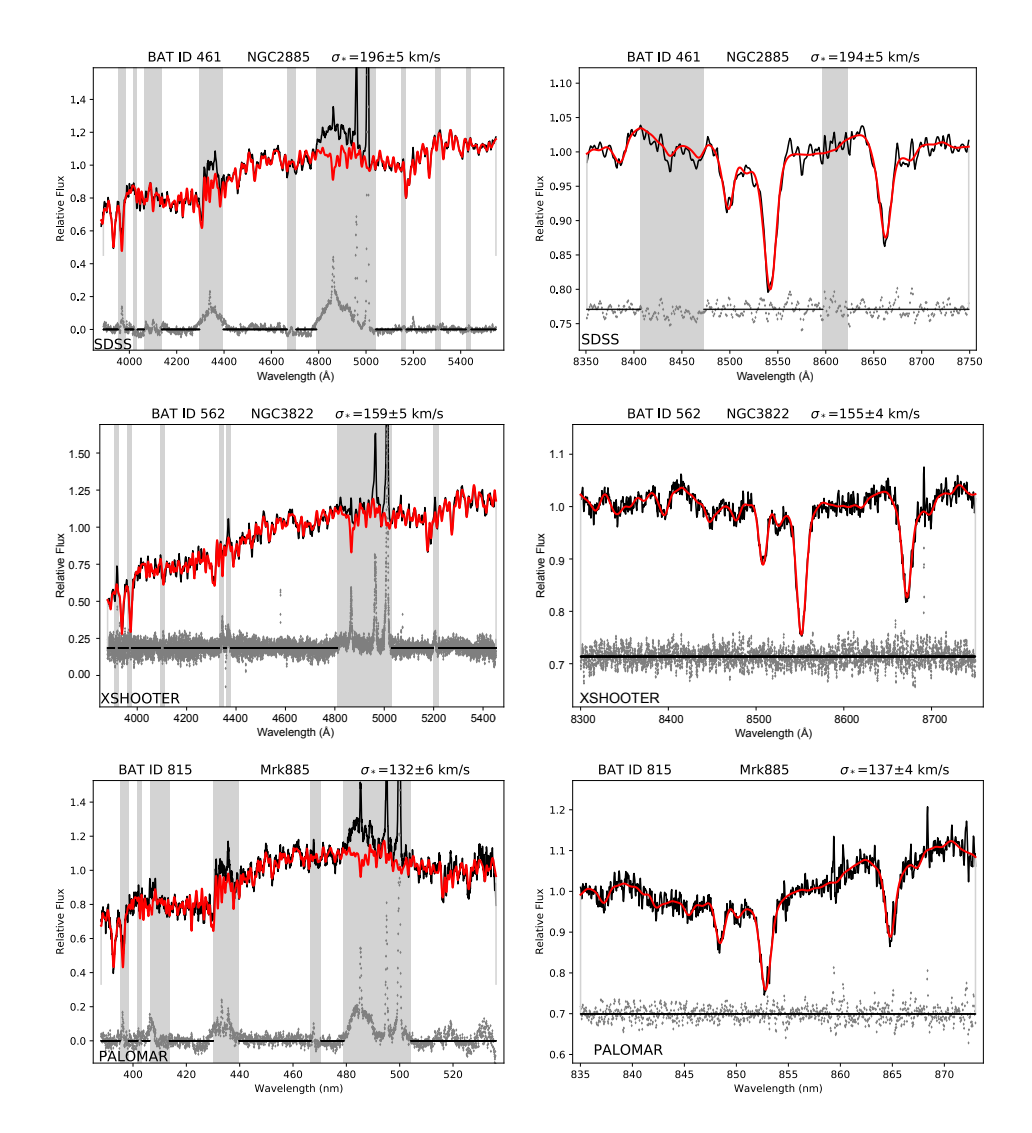


Figure 6.13: Examples of the successful σ_{Blue} (left panels) and σ_{Red} (right panels) fitting plots for SDSS, VLT/X-shooter, and Palomar/Double Spectrograph data (from top to bottom).

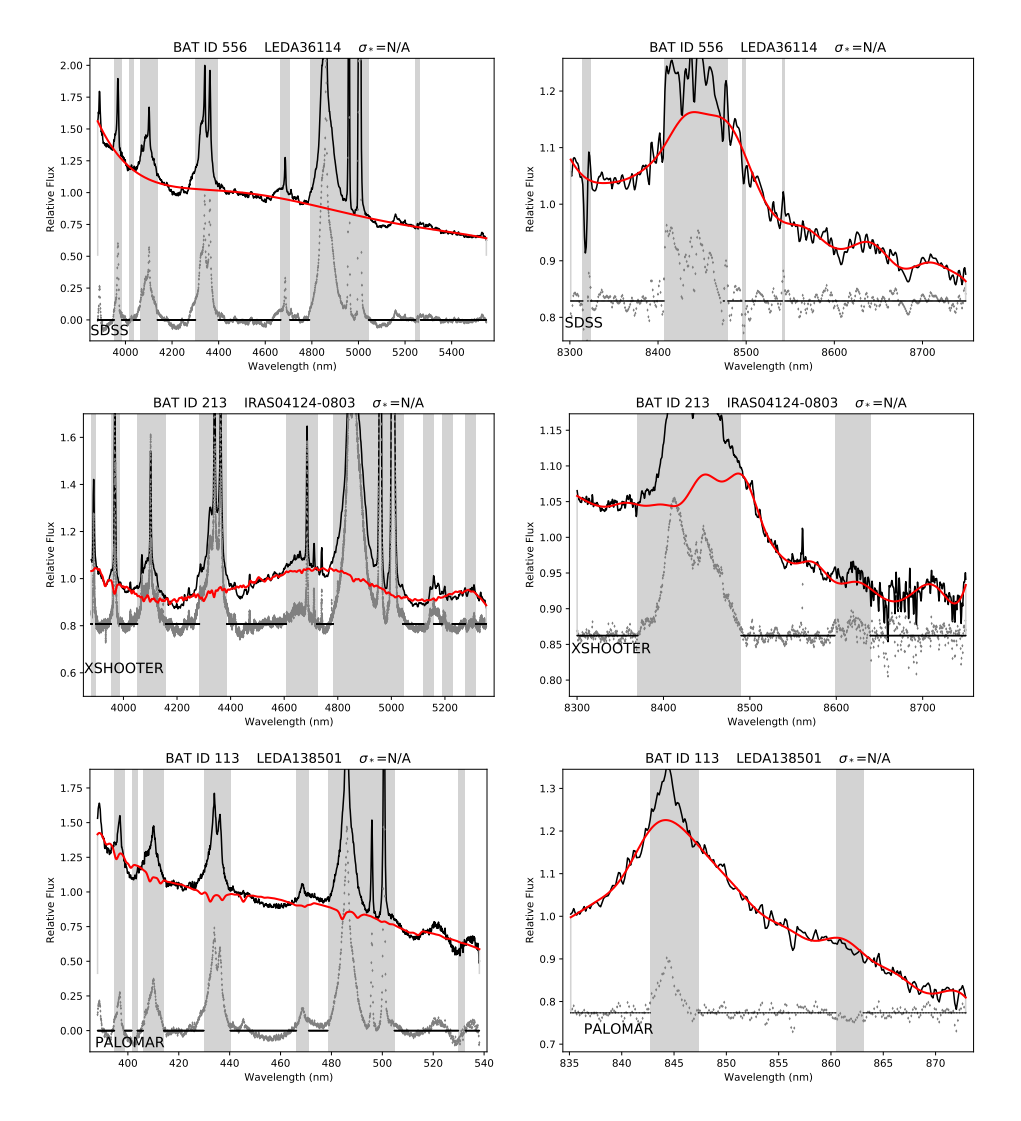


Figure 6.14: Examples of the failed σ_{Blue} (**left panels**) and σ_{Red} (**right panels**) fitting plots for SDSS, VLT/X-shooter, and Palomar/Double Spectrograph data (from top to bottom)

Table 6.3. The Spearman rank-order correlation results. The table is presented with a color code of ρ values for visual aid. Black, blue and red colors correspond to p-value ≤ 0.01 , p-value ≤ 0.05 , and p-value > 0.05, respectively. Units are as follows, σ_* and FWHM values are in km s⁻¹, luminosities are in erg s⁻¹, $M_{\rm BH}$ values are in M \odot , $N_{\rm H}$ is in cm⁻² and $A_{\rm V}$ is in mag.

		(1 1	DIV 11 11	ll	7	3.6	EW UM	7	3.5	V	¥	1	1	1001	717
	*	(z + 1)	F W Π MH β	$_{ m TH}_{ m B}$	L5100	$^{MBH,H\beta}$	$FWHWH\alpha$	$_{ m CH}_{ m G}$	$MBH,H\alpha$	HAT	ΑV	$L_{\rm Edd}$	L_{Bol}	IOS AEdd	Δ_{MBH}
σ_{\star}	1	0.4	0.58	0.33	0.37	0.63	0.54	0.36	0.57	-0.12	-0.04	0.57	0.52	-0.21	-0.27
$\log(1+z)$	0.4	—	0.24	0.59	0.62	0.52	0.27	69.0	9.0	-0.12	0.38	9.0	0.82	90.0	0.38
$FWHM_{ m Heta}$	0.58	0.24	1	0.04	0.12	0.82	0.77	0.07	0.58	-0.08	-0.23	0.58	0.26	-0.5	0.17
$L_{{ m H}eta}$	0.33	0.59	0.04	1	0.89	0.56	0.25	0.91	29.0	-0.16	0.51	0.67	69.0	-0.21	0.45
L_{5100}	0.37	0.62	0.12	0.89	1	0.58	0.26	0.83	0.63	-0.15	0.46	0.64	0.63	-0.22	0.36
$M_{ m BH,H}_{eta}$	0.63	0.52	0.82	0.56	0.58		0.74	0.55	0.84	-0.16	60.0	0.84	0.58	-0.51	0.38
$FWHM_{ m Hlpha}$	0.54	0.27	0.77	0.25	0.26	0.74	1	0.23	8.0	-0.11	-0.03	8.0	0.34	-0.73	0.35
$L_{ m Hlpha}$	0.36	0.69	0.07	0.91	0.83	0.55	0.23	1	0.73	-0.15	0.56	0.73	0.79	-0.16	0.47
$M_{ m BH,H}{}_{lpha}$	0.57	9.0	0.58	0.67	0.63	0.84	8.0	0.73		-0.15	0.32	1	69.0	-0.58	0.53
$N_{ m H}$	-0.12	-0.12	-0.08	-0.16	-0.15	-0.16	-0.11	-0.15	-0.15	1	-0.04	-0.15	-0.09	0.13	90.0-
$A_{ m V}$	-0.04	0.38	-0.23	0.51	0.46	60.0	-0.03	0.56	0.32	-0.04		0.32	80.0	-0.4	-0.35
$L_{ m Edd}$	0.57	9.0	0.58	0.67	0.64	0.84	8.0	0.73	П	-0.15	0.32	1	69.0	-0.59	0.53
$L_{ m Bol}$	0.52	0.82	0.26	69.0	0.63	0.58	0.34	0.79	69.0	-0.09	80.0	0.69	1	0.1	0.23
$\log \lambda_{ m Edd}$	-0.21	90.0	-0.5	-0.21	-0.22	-0.51	-0.73	-0.16	-0.58	0.13	-0.4	-0.59	0.1	1	-0.46
$\Delta M_{ m BH}$	-0.27	0.38	0.17	0.45	0.36	0.38	0.35	0.47	0.53	-0.06	-0.35	0.53	0.23	-0.46	1

NOTE— $\Delta_{\text{MBH}},~L_{\text{Bol}}$ and $\log \lambda_{\text{Edd}}$ are computed using the following formulas:

 $\Delta M_{
m BH} = log M_{
m BH,\sigma}$ - $log M_{
m BH,BLR}$

 $L_{
m Bol} = 8 \times L_{
m X, 14-195 \, keV}$

 $\log \lambda_{\rm Edd} = L_{\rm Bol} \; / \; (1.26 {\rm E} + 38 \, \times \, M_{\rm BH,BLR})$